Supplementary Information
Measuring Relative Coupling Strength in Circadian Systems

Christoph Schmal * Erik D. Herzog † Hanspeter Herzel ‡

1 Supplementary Text

1.1 Lessons from the Kuramoto Model

The synchronization behavior of weakly interacting oscillators with finite amplitude can often be adequately approximated by means of a phase description [1]. Such phase oscillator model can be described via

$$\frac{\mathrm{d}\theta_i}{\mathrm{d}t} = \omega_i + \sum_{j=1}^{N} H_{ij}(\theta_j - \theta_i) \tag{1}$$

where θ_i is the time-dependent phase of oscillator i and $H_{ij}(\theta_j - \theta_i)$ is the coupling function between oscillator j and i. Here we study the Kuramoto model, defined by an isotropic sinusoidal all-to-all interaction between the oscillators given by

$$H_{ij}(\theta_j - \theta_i) = \frac{K}{N}\sin(\theta_j - \theta_i) \tag{2}$$

where K denotes the coupling coefficient [2]. In the thermodynamic limit of many oscillators, i.e., $N \to \infty$, we can reformulate Equation (1) as

$$v(\theta, \omega, t) = \omega + K \int_0^{2\pi} f(\theta', \omega, t)\, \sin(\theta' - \theta)\, d\theta'\, d\omega\,. \tag{3}$$

where $v(\theta, \omega, t)$ is the phase velocity at a certain phase position θ at time t, given that its natural frequency equals ω, and $f(\theta, \omega, t)\,\mathrm{d}\theta\,\mathrm{d}\omega$ is the fraction of oscillators in the phase and frequency ranges $[\theta, \theta + \mathrm{d}\theta]$ and $[\omega, \omega + \mathrm{d}\omega]$, respectively [3]. From the conservation of oscillators with a given ω follows the continuity equation

$$\frac{\partial f}{\partial t} + \partial_\theta[fv] \stackrel{!}{=} 0 \tag{4}$$

that determines the temporal evolution of distribution f. Expanding the density $f(\omega, \theta, t)$ into its Fourier series

$$f(\omega, \theta, t) = \frac{g(\omega)}{2\pi}\left[1 + \sum_{n=1}^{\infty} f_n(\omega, t)e^{i\,n\,\theta} + \bar{f}_n(\omega, t)e^{-i\,n\,\theta}\right] \tag{5}$$

*Institute for Theoretical Biology, Charité - Universitätsmedizin, Philippstr. 13, D-10115 Berlin
†Department of Biology, Washington University in St. Louis, St. Louis, MO 63130
‡Institute for Theoretical Biology, Humboldt Universität zu Berlin, Invalidenstr. 42, D-10115 Berlin

and choosing the *Ott-Antonsen Ansatz*

$$f_n(\omega, \theta, t) = \alpha^n(\omega, t) \tag{6}$$

as proposed by *E. Ott* and *T. M. Antonsen* [4], we can show that the complex conjugate of the order parameter

$$z(t) = \langle e^{i\,\theta} \rangle_f = \int_{\mathbb{R}} \int_0^{2\pi} e^{i\,\theta} f(\theta, \omega, t)\, d\theta\, d\omega \tag{7}$$

can be written as

$$\bar{z}(t) = \int_{\mathbb{R}} d\omega\, g(\omega)\, \alpha(\omega, t)\,. \tag{8}$$

Inserting Equation (5) together with (6) into Equation (4) we find that the Ott-Antonsen Ansatz solves Equation (4) if

$$\frac{\partial \alpha}{\partial t} + \frac{K}{2}(z\,\alpha^2 - \bar{z}) + i\,\omega\alpha = 0\,. \tag{9}$$

Assuming that the oscillators intrinsic frequencies follow a Cauchy-Lorentz distribution

$$g(\omega) = \frac{\kappa}{\pi\left[(\omega - \omega_0)^2 + \kappa^2\right]} \tag{10}$$

where ω_0 and κ denote the center and the scale parameter of the distribution, respectively, one can show that

$$\bar{z}(t) = \alpha(\omega = \omega_0 - i\,\kappa, t) \tag{11}$$

which consequently leads to

$$\frac{\partial z}{\partial t} + \frac{K}{2} z(|z|^2 - 1) + \kappa z = 0\,. \tag{12}$$

Interpreting z by means of polar coordinates $z = Re^{i\psi}$, we obtain

$$\frac{\partial R}{\partial t} + \frac{K}{2} R^3 + R\left(\kappa - \frac{K}{2}\right) = 0 \tag{13}$$

for the dynamical evolution of the time-dependent phase coherence $R(t)$. Equation (13) can be solved numerically and analytically. A linear stability analysis reveals that the incoherent state $R_1^\star = 0$ is stable for

$$K < K_c = 2\kappa\,, \tag{14}$$

and that the phase coherence stably reaches a value of

$$R_2^\star = \sqrt{1 - \frac{2\kappa}{K}} \tag{15}$$

for $K > K_c = 2\kappa$. In Supplementary Figure S3 we plot $R_2^\star$ against K for different scale parameters κ. Note that the above calculations resemble those of Reference [4] for arbitrary values of κ. In [4], κ was set to one.

1.2 Analytical Approximation of Amplitude Expansion Effects

In order to find an approximation for the amplitude expansion upon mutual mean-field coupling in an ensemble of N Poincaré oscillators we make the following assumptions: First, we assume that the dynamics

$$\frac{\mathrm{d}x_i}{\mathrm{d}t} = \gamma_i\, x_i(A_i - r_i) - \frac{2\,\pi}{\tau_i} y_i + \frac{K}{N}\sum_{i=1}^{N} x_i(t) \tag{16}$$

$$\frac{\mathrm{d}y_i}{\mathrm{d}t} = \gamma_i\, y_i(A_i - r_i) + \frac{2\,\pi}{\tau_i} x_i \tag{17}$$

of the network, as defined by Equations (11)–(12) in Section *Model Equations* of the Main Text, is similar to the radially symmetric dynamics defined by

$$\frac{\mathrm{d}x_i}{\mathrm{d}t} = \gamma_i\, x_i(A_i - r_i) - \frac{2\,\pi}{\tau_i} y_i + \frac{K}{2N}\sum_{i=1}^{N} x_i(t) \tag{18}$$

$$\frac{\mathrm{d}y_i}{\mathrm{d}t} = \gamma_i\, y_i(A_i - r_i) + \frac{2\,\pi}{\tau_i} x_i + \frac{K}{2N}\sum_{i=1}^{N} y_i(t)\,. \tag{19}$$

Second, we make the following considerations based on symmetries of the system: Recall that we have assumed in the Main Text that every oscillator has a fixed amplitude $A_i = A$ and a fixed radial relaxation rate $\gamma_i = \gamma$ while individual oscillators differ only with respect to their free-running period τ_i, sampled from a normal distribution with mean μ_τ and standard deviation σ_τ. From symmetry reasons one could now speculate that the amplitude expansion of the ensemble will be analogous to the amplitude expansion of two mean field coupled oscillators with amplitudes A, radial relaxation rates γ, and different internal periods $\tau_1 = \mu_\tau - \sigma_\tau$ and $\tau_2 = \mu_\tau + \sigma_\tau$. For this two-oscillator case, we can determine the amplitude expansion analytically. To this end, we rewrite Equations (18)–(19) for $N = 2$ in polar coordinates, i.e.,

$$\frac{\mathrm{d}r_1}{\mathrm{d}t} = \gamma r_1(A - r_1) + \frac{K}{4}(r_1 + r_2\cos(\Delta\theta)) \tag{20}$$

$$\frac{\mathrm{d}r_2}{\mathrm{d}t} = \gamma r_2(A - r_2) + \frac{K}{4}(r_2 + r_1\cos(\Delta\theta)) \tag{21}$$

$$\frac{\mathrm{d}\theta_2}{\mathrm{d}t} - \frac{\mathrm{d}\theta_1}{\mathrm{d}t} = \Delta\omega - \frac{K}{4}\left[\frac{r_1}{r_2} + \frac{r_2}{r_1}\right]\sin(\Delta\theta) \tag{22}$$

with $\Delta\theta := \theta_2 - \theta_1$ and $\Delta\omega := \omega_2 - \omega_1$. Restricting ourselves to stationary solutions with $r_1 = r_2 =: r$ in the phase-locked regime as defined by $\frac{\mathrm{d}\Delta\theta}{\mathrm{d}t} = 0$, the amplitude r of both oscillators in case of overcritical coupling reads as

$$r = A + \frac{K}{4\gamma}\left(1 + \sqrt{1 - \left(\frac{2\Delta_\omega}{K}\right)^2}\right)\,. \tag{23}$$

Numerical simulations reveal a good agreement between this amplitude r and the mean $\mu_A(K)$ of the amplitude distribution in the full system, consisting of N oscillators in case of overcritical coupling.

Note, that deviations of the analytical approximation and the simulation results, as can be observed in Figure 4 C of the Main Text, originate from a slightly different definition of the mean field and how it couples to the individual oscillators. Comparing r with numerically estimated values of μ_A for an integration of system (18)-(19) reveals an almost perfect overlap of r and μ_A, see Supplementary Figure S4. However, due to the fact that dynamical systems as defined by Equations

(16)-(17) have been widely used in theoretical studies of circadian systems [5–7], we nevertheless choose to investigate numerical solutions of system (16)-(17) instead of those regarding to system (18)-(19), even if the latter is easier to treat analytically due to its symmetric nature.

Finally, it should be noted that a similar analysis can be applied to oscillator types with radial dynamics that deviate from those of the Poincaré oscillator. In case of the *linearized Hopf oscillator* or the *Hopf oscillator* where the dynamics of a single (uncoupled) oscillator in Cartesian coordinates reads as

$$\frac{\mathrm{d}x_i}{\mathrm{d}t} = \gamma_i \frac{x_i}{r_i}(A_i - r_i) - \frac{2\,\pi}{\tau_i} y_i \tag{24}$$

$$\frac{\mathrm{d}y_i}{\mathrm{d}t} = \gamma_i \frac{y_i}{r_i}(A_i - r_i) + \frac{2\,\pi}{\tau_i} x_i \tag{25}$$

and

$$\frac{\mathrm{d}x_i}{\mathrm{d}t} = \gamma_i\, x_i(A_i - r_i^2) - \frac{2\,\pi}{\tau_i} y_i \tag{26}$$

$$\frac{\mathrm{d}y_i}{\mathrm{d}t} = \gamma_i\, y_i(A_i - r_i^2) + \frac{2\,\pi}{\tau_i} x_i\,, \tag{27}$$

respectively, we can approximate the mean $\mu_A(K)$ of the amplitude distribution in case of symmetrical mean field coupling as

$$\mu_A^{\text{Linearized Hopf}}(K) = \frac{A}{1 - \frac{K}{4\gamma}\left(1 + \sqrt{1 - \left(\frac{2\Delta_\omega}{K}\right)^2}\right)} \tag{28}$$

and

$$\mu_A^{\text{Hopf}}(K) = \sqrt{A + \frac{K}{4\gamma}\left(1 + \sqrt{1 - \left(\frac{2\Delta_\omega}{K}\right)^2}\right)}\,, \tag{29}$$

respectively. Again, a good agreement between the analytical approximations and numerical simulations can be observed in case of overcritical coupling, see Supplementary Figures S14 and S15 (blue dashed lines).

2 Supplementary Figures

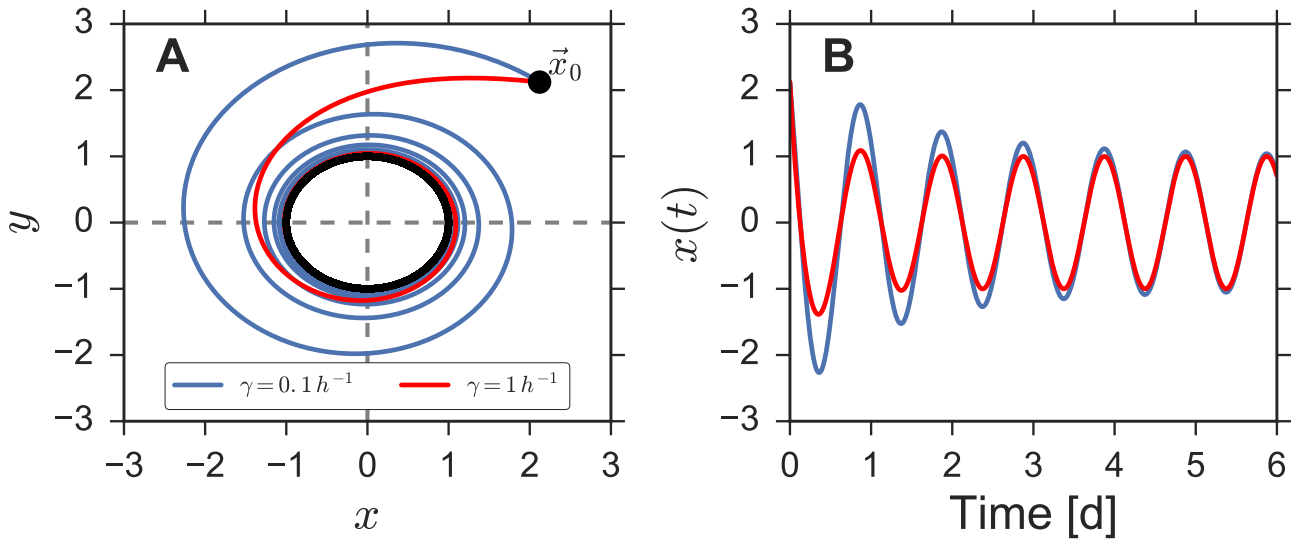

Figure S1. Graphical illustration of the Poincaré oscillator. A) Solution of Equations (9)–(10) of the Main Text for $A = 1$, $\tau = 24$h and two different radial relaxation rates $\gamma = 0.1\text{h}^{-1}$ (blue line) and $\gamma = 1\text{h}^{-1}$ (red line), respectively, plotted in the $x - y$ plane. Initial conditions (black dot) are given by $r_0 = 3$ and $\theta_0 = 45°$, i.e., $x_0 = r_0 \cos(\theta_0)$ and $y_0 = r_0 \sin(\theta_0)$. Note that the radial relaxation rate γ determines, how fast a perturbation from the steady state amplitude (black line) relaxes back to the limit cycle dynamics. B) Corresponding dynamics of variable $x(t)$, plotted in an $x - t$ diagram.

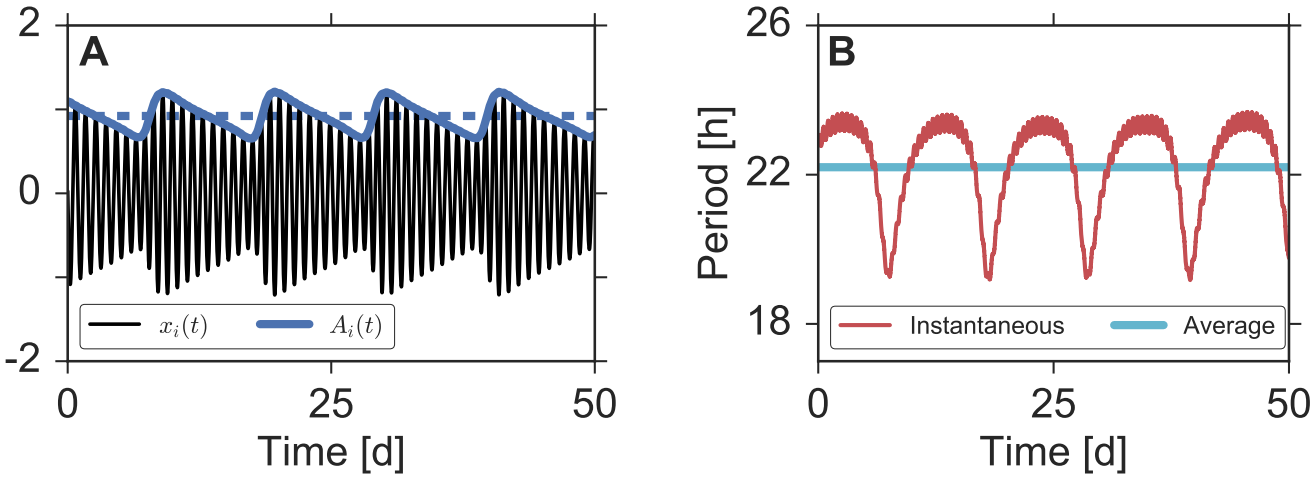

Figure S2. Example analysis of a simulated time series showing beating behavior. Here, we illustrate the numerical determination of amplitudes and periods by means of a Hilbert transformation as described in Section *Materials and Methods* of the Main Text. A) The oscillatory time series $x_i(t)$ (black line) corresponds to an oscillatory solution from Figure 1B of the Main Text. $A_i(t)$ denotes the corresponding instantaneous amplitude, determined by means of a Hilbert transformation. Histograms in Figure 3 C of the Main Text are based on the mean values (dashed blue line) of $A_i(t)$. B) Instantaneous period (red line) of the oscillatory time series from panel (A), determined by a numerical differentiation of the instantaneous phase $\theta_i(t)$, in comparison with the corresponding average period $\langle \tau_i^{\text{HT}} \rangle$, determined as described in Section *Materials and Methods* of the Main Text.

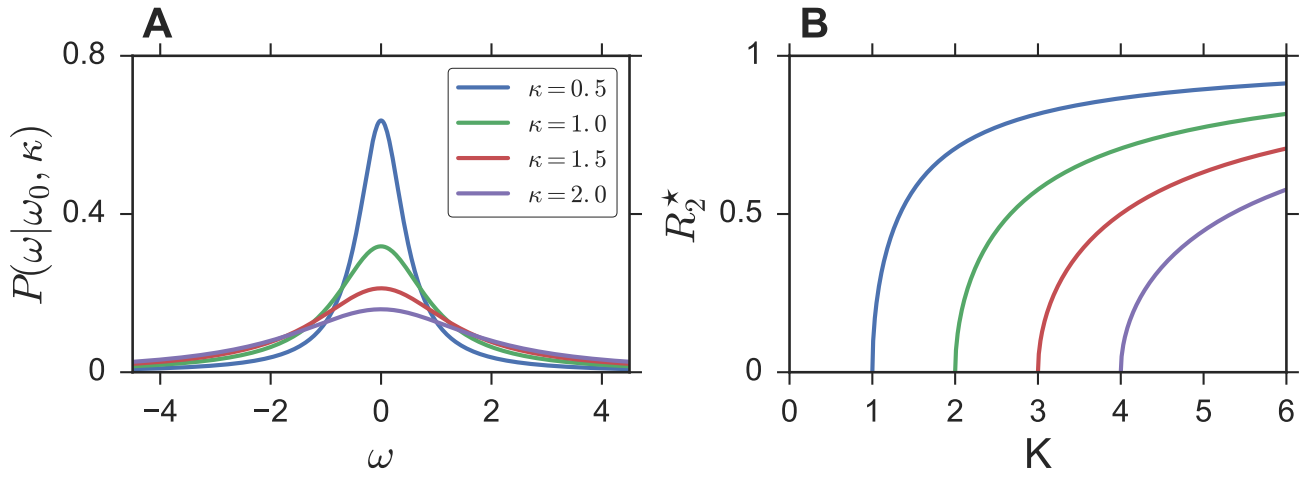

Figure S3. Emergent network properties in the Kuramoto model. A) Examples of the Cauchy-Lorentz distribution with median $\omega_0 = 0$ and different *scale parameters* κ as defined by Equation (10). B) Steady state order parameter $R_2^\star$ of the partially synchronized state, given by Equation (15), is plotted against coupling strength K for different values of scale parameters κ.

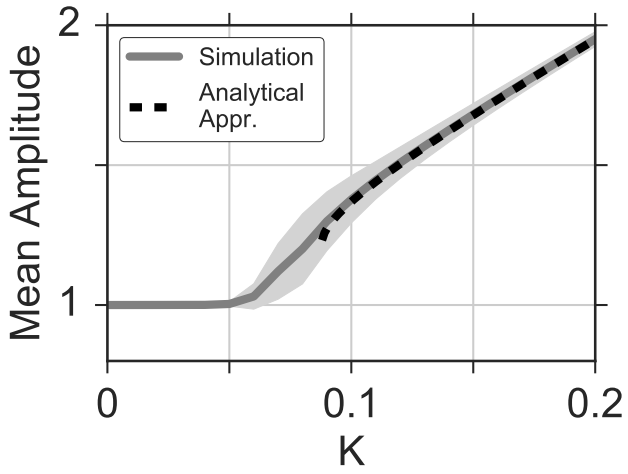

Figure S4. Analytical approximation of amplitude expansion in the radially symmetric system. Here we show that the analytical approximation of the amplitude expansion (dashed black line), as given by Equation (13) of the Main Text or Equation (23) of Supplementary Text 1.2, yields an almost perfect agreement with the mean value (bold gray line) of the amplitude distribution as determined by simulations of the radially symmetric system, given by Equations (18)-(19) of Supplementary Text 1.2, in case of overcritical coupling. Standard deviations of the simulated amplitude distributions are depicted by gray shaded areas. In correspondence to Figure 4 C of the Main Text, single cell oscillator parameters of $A_i = 1$, $\gamma_i = 0.1\text{h}^{-1}$, $\mu_\tau = 24\text{h}$, and $\sigma_\tau = 2\text{h}$ have been used for numerical simulations.

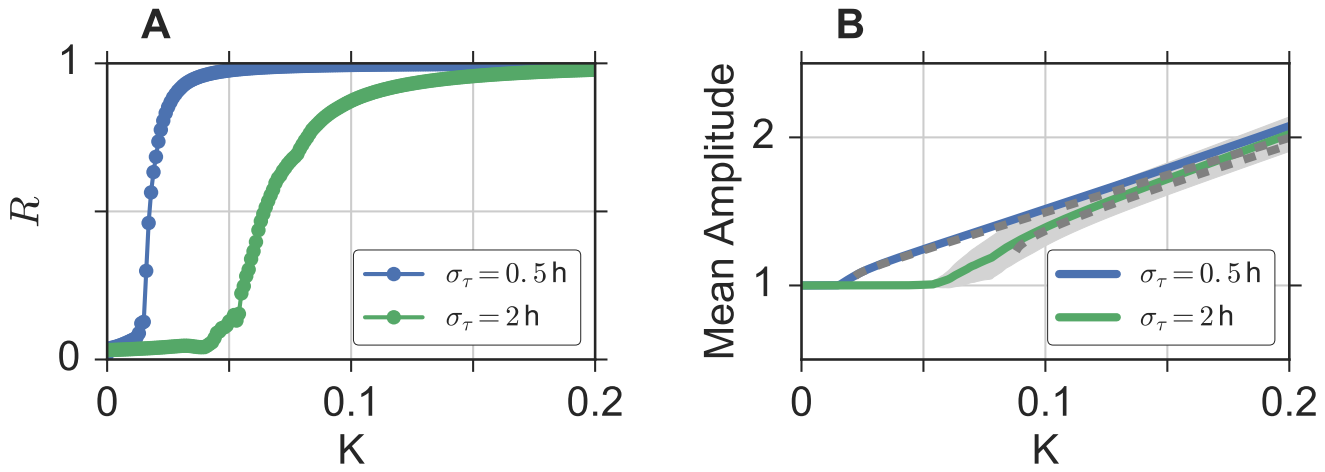

Figure S5. Emergent phenomena depend on single cell oscillator properties: Dependence on the period spread σ_τ. Other oscillator parameters have been set to the same values as in Figures 1–4 of the Main Text, i.e., $A = 1$ and $\mu_\tau = 24\,\mathrm{h}$, and $\gamma = 0.1\,\mathrm{h}^{-1}$.

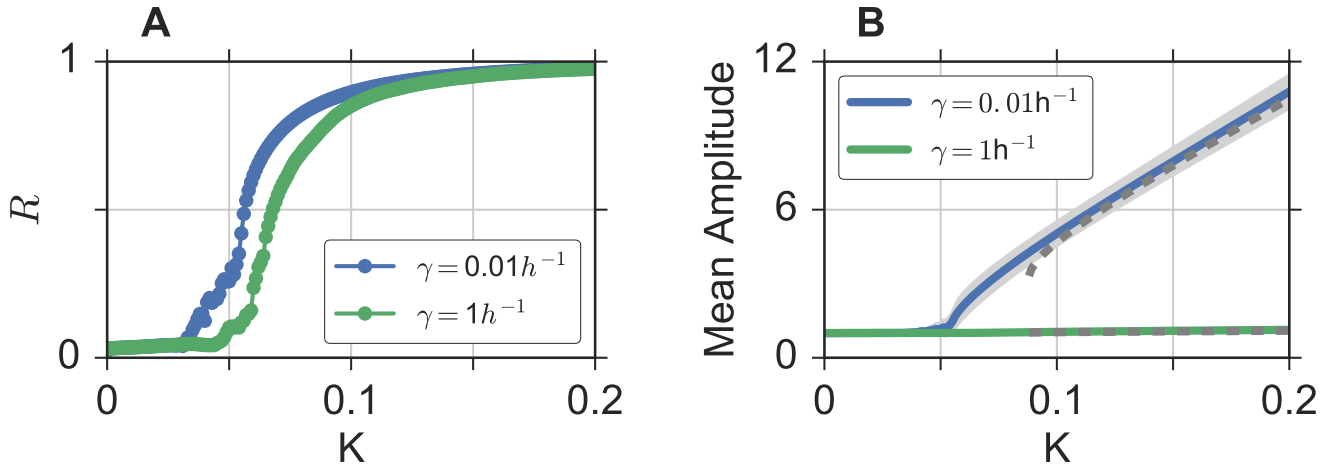

Figure S6. Emergent phenomena depend on single cell oscillator properties: Dependence on the radial relaxation rate γ. Other oscillator parameters have been set to the same values as in Figures 1–4 of the Main Text, i.e., $A = 1$, $\mu_\tau = 24\,\mathrm{h}$, and $\sigma_\tau = 2\,\mathrm{h}$.

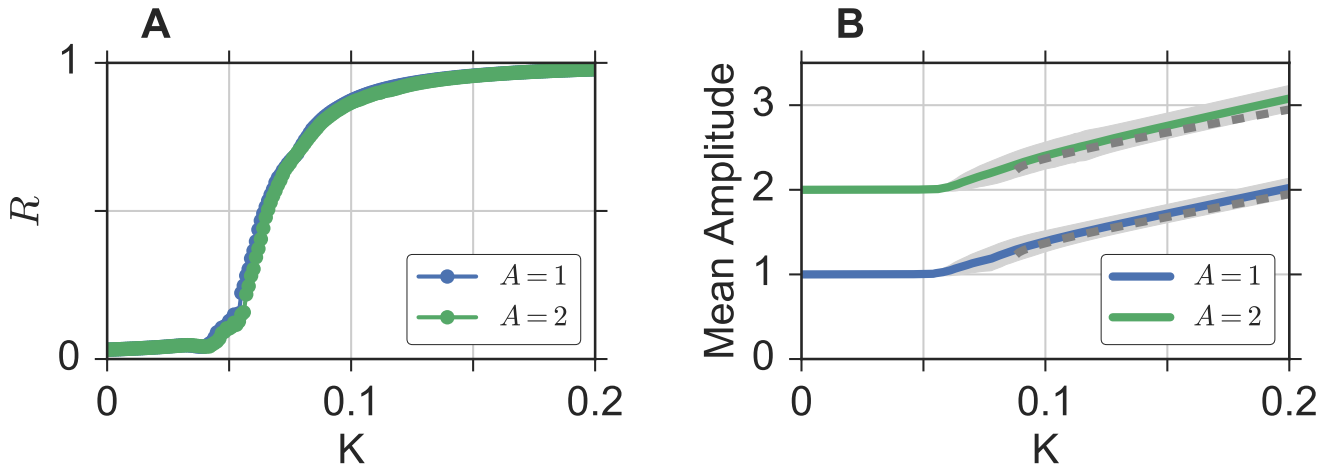

Figure S7. Emergent phenomena depend on single cell oscillator properties: Dependence on the amplitude A. Other oscillator parameters have been set to the same values as in Figures 1–4 of the Main Text, i.e., $\gamma = 0.1\,\mathrm{h}^{-1}$, $\mu_\tau = 24\,\mathrm{h}$, and $\sigma_\tau = 2\,\mathrm{h}$.

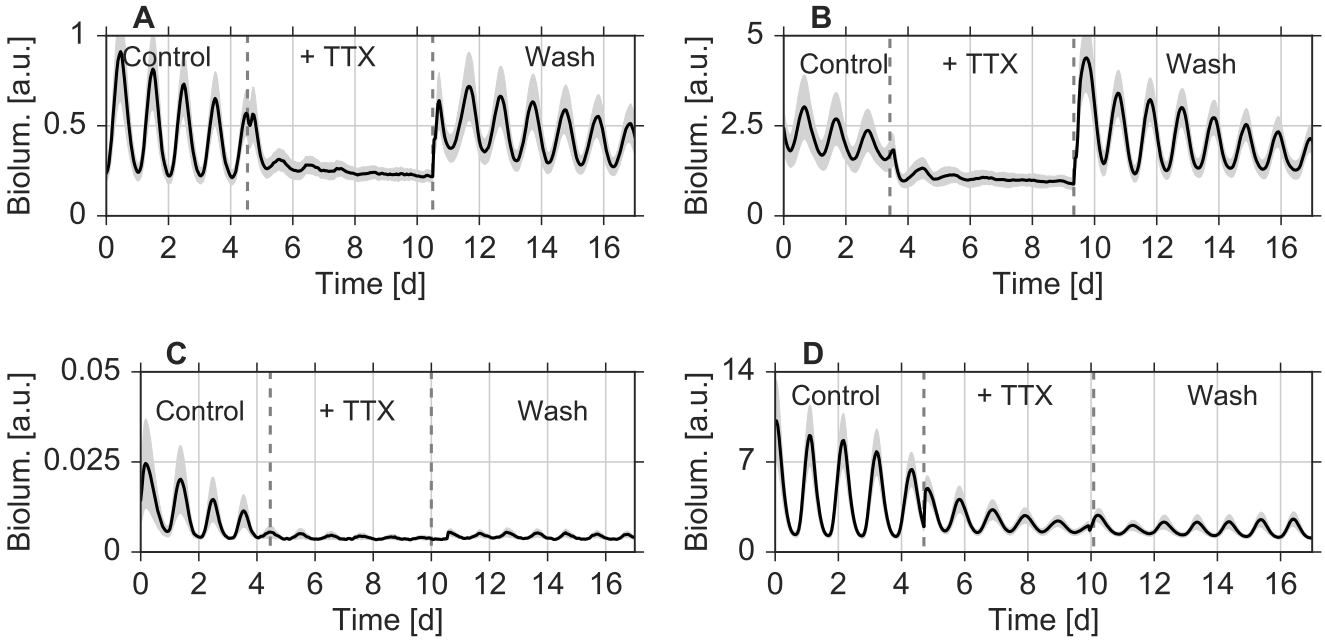

Figure S8. Time series data of four different SCN slices. Ensemble averages (black lines) and standard deviations (gray shaded areas) of bioluminescence time-series from automatically identified and tracked neurons in four coronal slices of the SCN as described in [8]. Experiments as depicted in panels A–D are replications of the experiment in Figure 5 A of the Main Text.

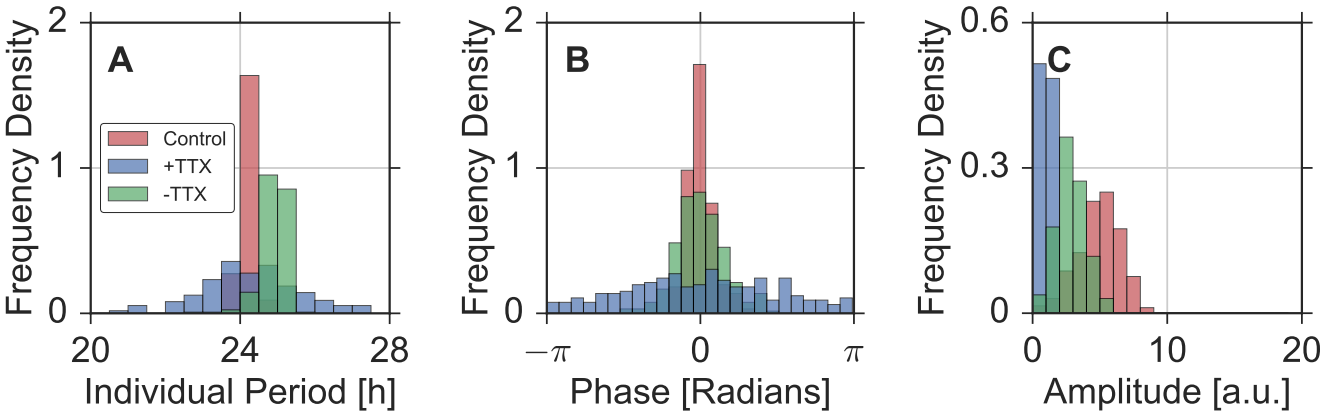

Figure S9. Emergent properties in SCN slice data. Same as Figure 6 of the Main Text, using data from SCN slice number two (SCN2). Statistical properties of the distributions are summarized in Supplementary Table S1–S3.

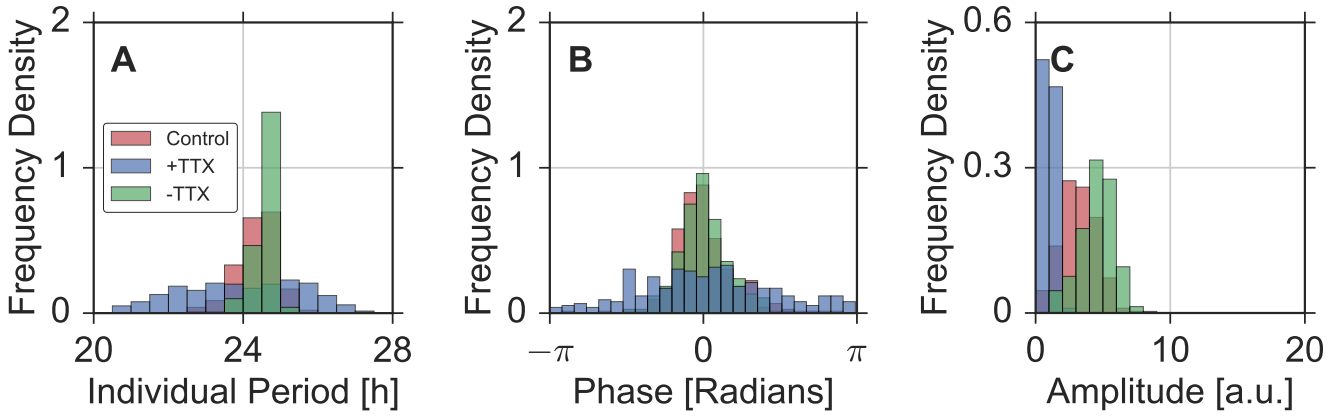

Figure S10. Emergent properties in SCN slice data. Same as Figure 6 of the Main Text, using data from SCN slice number three (SCN3). Statistical properties of the distributions are summarized in Supplementary Table S1–S3.

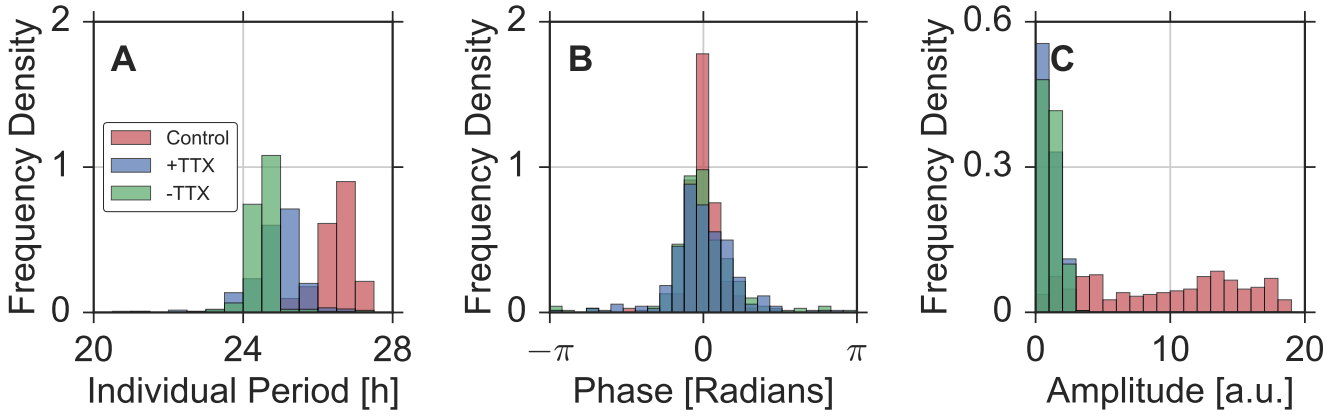

Figure S11. Emergent properties in SCN slice data. Same as Figure 6 of the Main Text, using data from SCN slice number four (SCN4). Statistical properties of the distributions are summarized in Supplementary Table S1–S3.

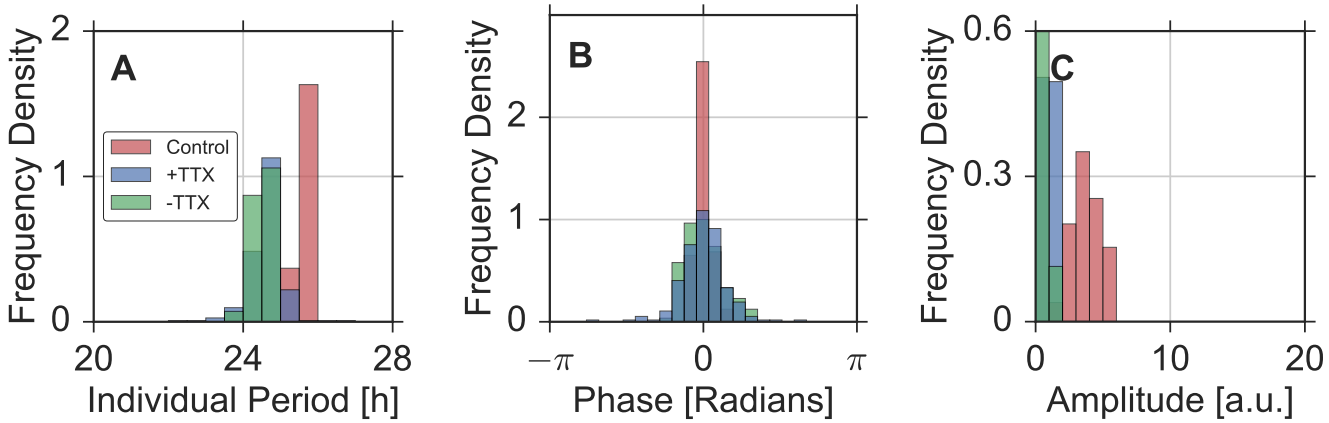

Figure S12. Emergent properties in SCN slice data. Same as Figure 6 of the Main Text, using data from SCN slice number five (SCN5). Statistical properties of the distributions are summarized in Supplementary Table S1–S3.

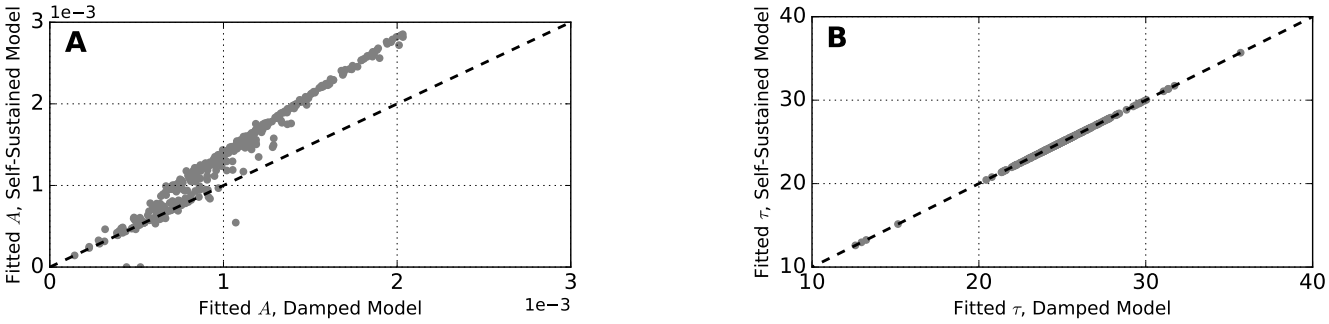

Figure S13. Comparison of two time series fitting approaches. Comparison of amplitude (A) and period (B) values as estimated by fitting a (stochastic) linearly damped oscillator (abscissa) or a self-sustained linearized Hopf oscillator (ordinate) to experimental time series data as described in the Main Text. The corresponding time series have been obtained from SCN1 under the application of TTX.

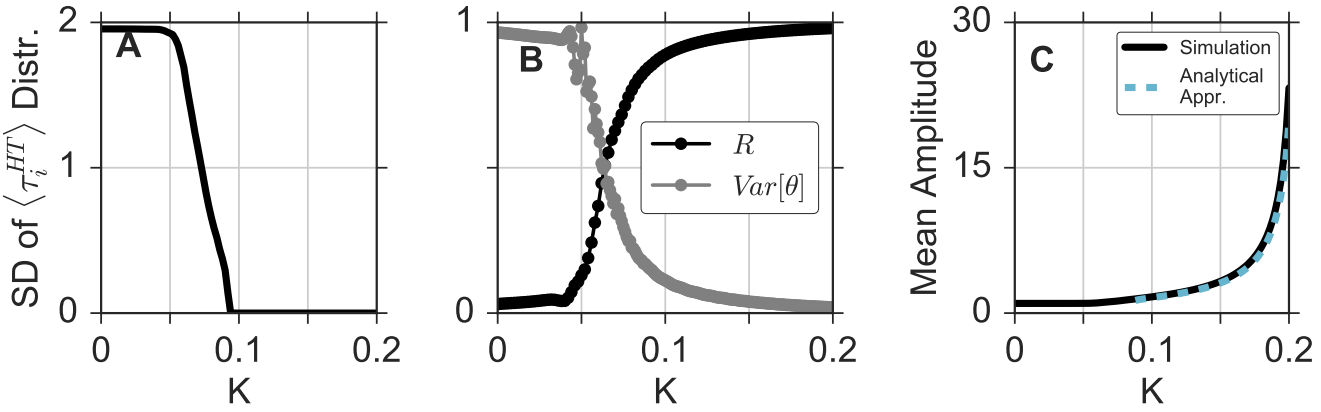

Figure S14. Dependence of emergent network properties on the coupling strength in case of a *linearized Hopf oscillator*. Same analysis as in Figure 4 of the Main Text, using a *linearized Hopf oscillator* as given by Equations (7)-(8) of the Main Text or Equations (24)-(25) of Supplementary Text 1.2. The dashed blue line denotes the analytical approximation of the mean value as given by Equation (28) of the Supplementary Information.

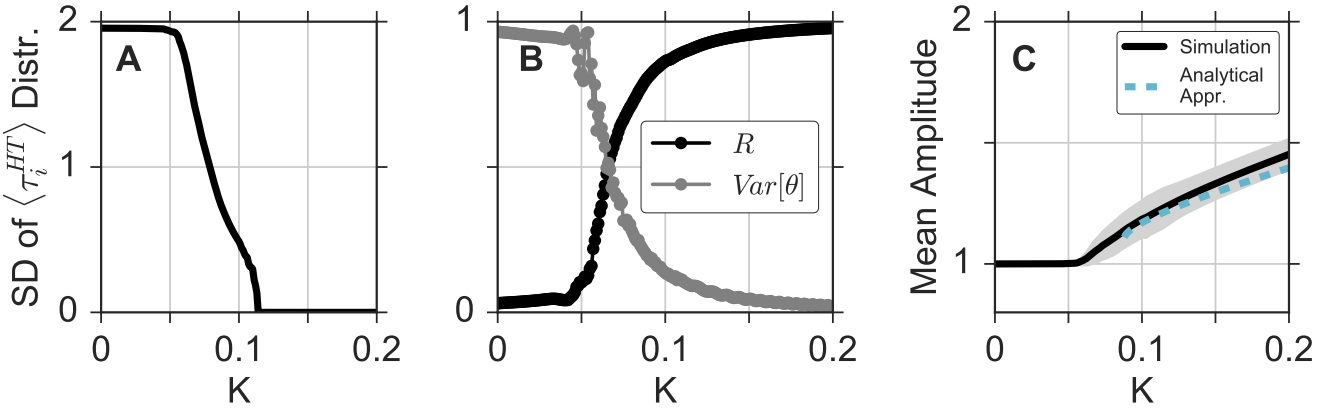

Figure S15. Dependence of emergent network properties on the coupling strength in case of a *Hopf oscillator*. Same analysis as in Figure 4 of the Main Text, using a *Hopf oscillator* as given by Equations (26)-(27) of Supplementary Text 1.2. The dashed blue line denotes the analytical approximation of the mean value as given by Equation (29) of the Supplementary Information.

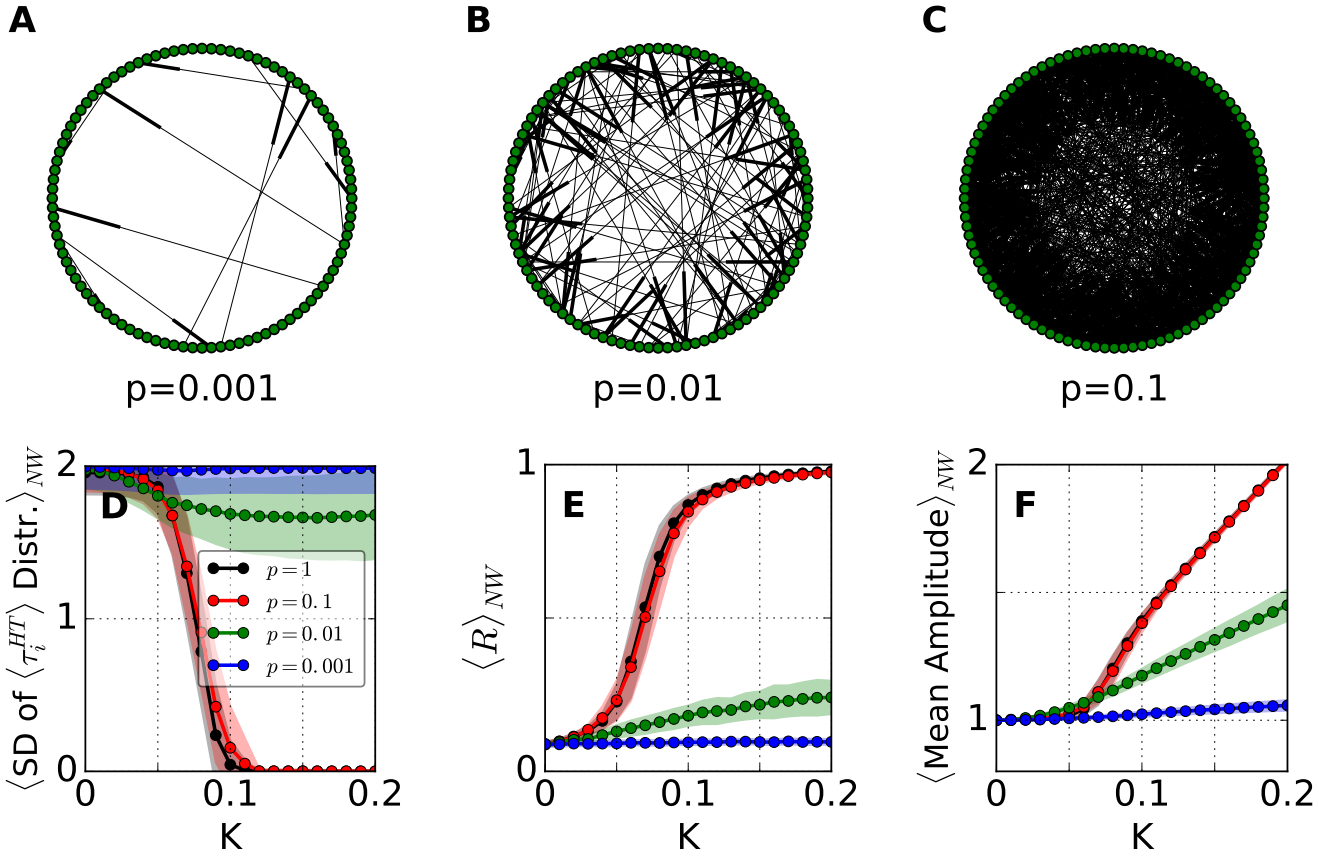

Figure S16. Emergent network properties of $N = 100$ randomly connected Poincaré oscillators. A-C) Examples of network topologies from a directed random graph with $N = 100$ nodes and different values of connection probabilities p. All graphs have been obtained as described in Section *Materials and Methods* of the Main Text. D-F) Same analysis as in Figure 4 A-C of the Main Text for $N = 100$ randomly connected Poincaré oscillators for different values of p. Note that each dot denotes the ensemble average $\langle \bullet \rangle_{NW}$ over 100 different randomly generated networks and the shaded areas depict the corresponding standard deviations.

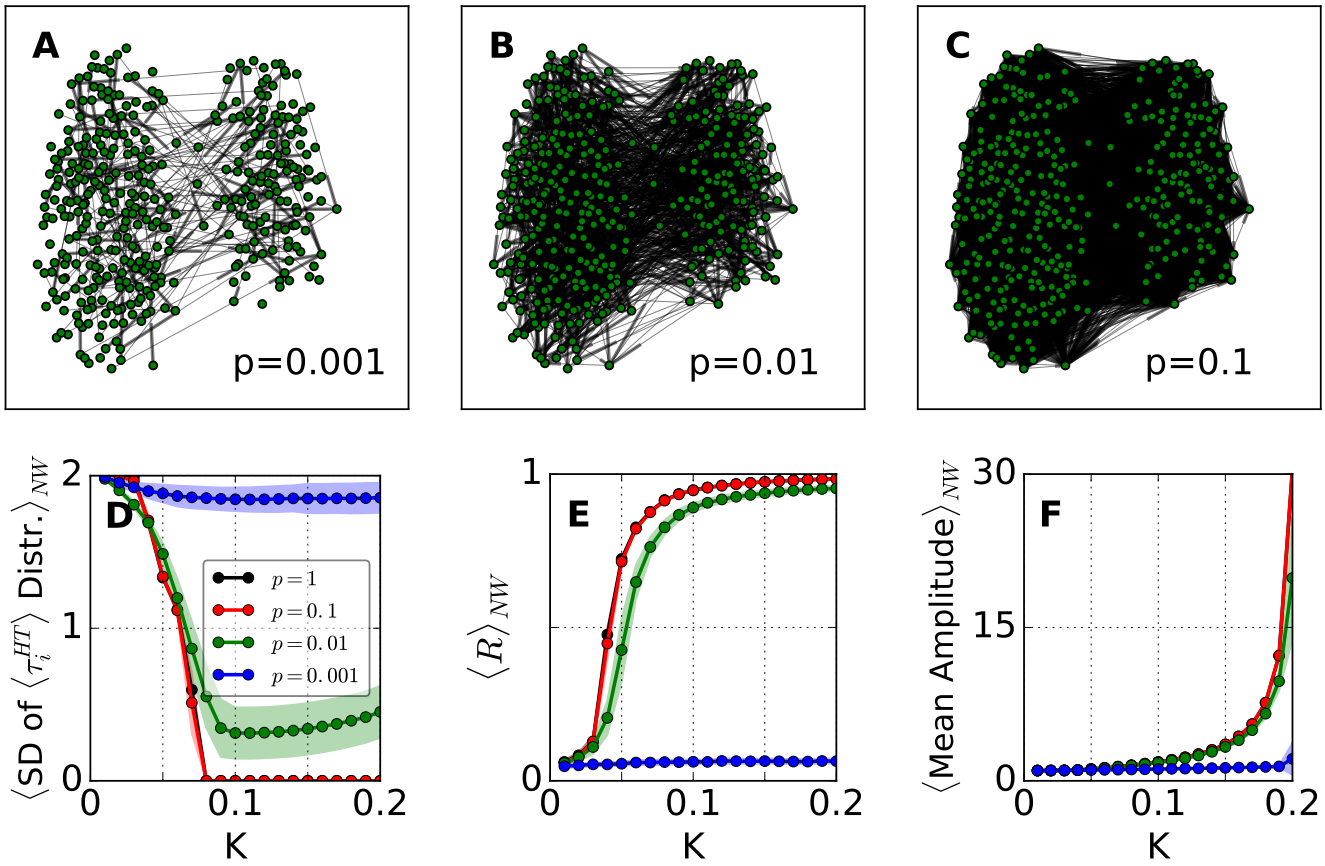

Figure S17. Emergent network properties of $N = 383$ randomly connected linearized Hopf oscillators. A-C) Examples of network topologies from a directed random graph with $N = 383$ nodes and different values of connection probabilities p where the location of the nodes corresponds to the locations of identified neurons in SCN1. All graphs have been obtained as described in Section *Materials and Methods* of the Main Text. Same as Supplementary Figure S16 for $N = 383$ randomly connected linearized Hopf oscillators where the period and amplitude values have been obtained from experimental time series data fits. Note that each dot denotes the ensemble average $\langle\bullet\rangle_{NW}$ over 50 different randomly generated networks and the shaded areas depict the corresponding standard deviations.

	Control			+ TTX			- TTX		
SCN #	μ_τ	s_τ	IQR_τ	μ_τ	s_τ	IQR_τ	μ_τ	s_τ	IQR_τ
SCN1	26.18	0.29	0.36	24.91	2.10	1.64	25.46	0.35	0.45
SCN2	24.20	0.20	0.23	25.06	2.50	2.19	23.41	5.85	0.40
SCN3	24.36	0.83	0.75	23.82	2.41	2.77	24.32	2.35	0.30
SCN4	26.36	1.77	0.54	23.34	5.00	0.92	24.18	2.25	0.29
SCN5	25.57	0.12	0.12	24.63	0.51	0.46	23.97	3.55	0.26

Table S1. Statistical properties of period distributions in SCN slice data. Mean values μ_τ, empirical standard deviations (s_τ), and interquartile ranges (IQR_τ) for period distributions under all three experimental conditions (Control, +TTX, -TTX) and all five SCN slice preparations (SCN1–SCN5). In some cases, outliers lead to large standard deviations, implying that interquartile ranges are more robust measures.

	Control		+ TTX		- TTX	
SCN #	$R(t_1)$	$Var[\theta(t_1)]$	$R(t_2)$	$Var[\theta(t_2)]$	$R(t_3)$	$Var[\theta(t_3)]$
SCN1	0.95	0.05	0.32	0.68	0.85	0.15
SCN2	0.97	0.03	0.26	0.74	0.88	0.12
SCN3	0.84	0.16	0.36	0.64	0.87	0.13
SCN4	0.94	0.05	0.83	0.17	0.83	0.17
SCN5	0.99	0.01	0.91	0.09	0.93	0.07

Table S2. Statistical properties of phase distributions in SCN slice data. Order parameter $R(t)$ and circular variances $Var[\theta(t)]$ in the distribution of phases at given time points $t_1 = 54\,\mathrm{h}$ (Control), $t_2 = 180\,\mathrm{h}$ (+TTX), and $t_3 = 365\,\mathrm{h}$ (-TTX), under all three experimental conditions (Control, +TTX, -TTX) for all five SCN slice preparations (SCN1–SCN5).

	Control			+ TTX			- TTX		
SCN #	μ_A	s_A	IQR_A	μ_A	s_A	IQR_A	μ_A	s_A	IQR_A
SCN1	11.78	3.44	4.89	1.0	0.40	0.52	5.67	1.89	2.73
SCN2	4.94	1.57	2.12	1.0	0.31	0.44	2.81	1.07	1.41
SCN3	3.21	1.33	1.91	1.0	0.33	0.43	4.55	1.27	1.51
SCN4	9.95	5.74	10.19	1.0	0.74	1.31	1.13	0.64	1.00
SCN5	3.79	1.03	1.64	1.0	0.34	0.47	0.68	0.26	0.39

Table S3: Statistical properties of amplitude distributions in SCN slice data. Mean values μ_A, empirical standard deviations (s_A), and interquartile ranges (IQR_A) for amplitude distributions under all three experimental conditions (Control, +TTX, -TTX) and all five SCN slice preparations (SCN1–SCN5).

References

[1] Yoshiki Kuramoto. *Chemical Oscillations, Waves, and Turbulence*. Dover Publications, Inc., Mineola, New York, 2003.

[2] Yoshiki Kuramoto. Self-entrainment of a population of coupled non-linear oscillators. In Prof Huzihiro Araki, editor, *International Symposium on Mathematical Problems in Theoretical Physics*, number 39 in Lecture Notes in Physics, pages 420–422. Springer Berlin Heidelberg, 1975.

[3] Steven H. Strogatz. From Kuramoto to Crawford: Exploring the onset of synchronization in populations of coupled oscillators. *Physica D*, 143(1-4):1–20, 2000.

[4] Edward Ott and Thomas M. Antonsen. Low dimensional behavior of large systems of globally coupled oscillators. *Chaos: An Interdisciplinary Journal of Nonlinear Science*, 18(3):037113, 2008.

[5] Ute Abraham, Adrian E Granada, Pal O Westermark, Markus Heine, Achim Kramer, and Hanspeter Herzel. Coupling governs entrainment range of circadian clocks. *Mol Syst Biol*, 6: 438, 2010.

[6] Changgui Gu, Jos H. T. Rohling, Xiaoming Liang, and Huijie Yang. Impact of dispersed coupling strength on the free running periods of circadian rhythms. *Phys Rev E*, 93(3):032414, 2016.

[7] Changgui Gu, Ming Tang, Jos H. T. Rohling, and Huijie Yang. The effects of non-self-sustained oscillators on the en-trainment ability of the suprachiasmatic nucleus. *Scientific Reports*, 6, 2016.

[8] John H. Abel, Kirsten Meeker, Daniel Granados-Fuentes, Peter C. St John, Thomas J. Wang, Benjamin B. Bales, Francis J. Doyle, Erik D. Herzog, and Linda R. Petzold. Functional network inference of the suprachiasmatic nucleus. *Proc Natl Acad Sci U S A*, 113(16):4512–4517, 2016.